Eur. Phys. J. Spec. Top.
https://doi.org/10.1140/epjs/s11734-025-01907-2

THE EUROPEAN PHYSICAL JOURNAL SPECIAL TOPICS

Regular Article

Quasistatic rheology of granular materials composed of dodecahedra

Duc Chung Vu[1,2,5,a], Lhassan Amarsid[1,b], Vincent Richefeu[3,c], Jean-Yves Delenne[4,d], and Farhang Radjai[2,e]

[1] CEA, DES, IRESNE, DEC, Cadarache, 13108 Saint-Paul-lez-Durance, France
[2] University of Montpellier, CNRS, LMGC, 163 rue Auguste Broussonnet, 34090 Montpellier, France
[3] 3SR, CNRS, University of Grenoble Alpes, 621 Avenue Centrale, 38400 Saint-Martin-d'Hères, France
[4] IATE, CIRAD, INRAE, Montpellier SupAgro, University of Montpellier, place Pierre Viala, 34060 Montpellier, France
[5] Present Address: Faculty of Hydraulic Engineering, Hanoi University of Civil Engineering, 55 Giai Phong Street, Hanoi, Vietnam

Received 24 August 2025 / Accepted 2 September 2025

Abstract Using three-periodic particle dynamics simulations, we investigate the microstructure of isotropic dense and loose packings of dodecahedral and spherical particles for different values of friction coefficient between particles. We also analyze the evolution of shear strength, packing fraction, particle connectivity, and anisotropy parameters under quasi-static triaxial compression. Our findings reveal that dodecahedral particles exhibit a wider range of packing fractions and a greater proportion of floating particles than spheres, highlighting the influence of interlocking and arching in these assemblies. The stress ratio, defined as the ratio of stress deviator to average stress, is nonzero even at zero friction and reaches higher values in dodecahedral packings compared to spherical ones. It increases with friction coefficient and eventually levels off at large friction coefficients. We show that the evolution of fabric and force anisotropies is strongly affected by friction coefficient and particle shape. Qualitative new features arising from non-spherical particle shape include (1) an enhanced ortho-radial force anisotropy, resulting from the combined effects of friction mobilization and the projection of normal forces on the branch vectors joining particle centers, (2) a negative branch vector length anisotropy, due to the alignment of face-to-face contacts with the compression axis, and (3) the distinct role of triple contacts in amplifying force anisotropy. Our findings suggest that the higher shear strength of packings of dodecahedral particles does not stem from a fundamentally different organization of the contact network, but rather from local force balance mechanisms induced by particle geometry. The stability of face–face contacts and their alignment with strong force chains account for the enhanced force anisotropy and shear strength observed in dodecahedral packings.

1 Introduction

Over the past 30 years, numerous studies on granular media have focused on model systems composed of spherical particles, using experiments with glass beads and discrete element method (DEM) simulations. While this simplification is significant compared to real granular materials, it is necessary to isolate generic collective behaviors [1, 2]. By "generic behavior", we refer to the overall rheological response governed by steric exclusions, friction, and inelastic collisions. Well-established granular phenomena—including Mohr–Coulomb behavior, stress–strain relationships, the influence of initial packing fraction, dilatancy, and inertial flow—are observed across materials of various particle shapes, including spheres [3]. However, macroscopic parameters such as the internal friction coefficient, the range of packing fraction variations, elastic moduli, and microscopic features like force chains and contact network anisotropy are highly sensitive to particle morphology [4–11].

[a] e-mail: chungvd@huce.edu.vn
[b] e-mail: lhassan.amarsid@cea.fr
[c] e-mail: vincent.richefeu@univ-grenoble-alpes.fr
[d] e-mail: jean-yves.delenne@umontpellier.fr
[e] e-mail: franck.radjai@umontpellier.fr (corresponding author)

Published online: 13 September 2025

Despite their critical role, the physical mechanisms by which particle morphology affects macroscopic properties remain poorly understood. This knowledge gap is largely due to the experimental challenges of obtaining particle-scale measurements and the limited availability of efficient DEM algorithms for non-spherical particles until recently. Advancements in technology, such as 3D printing of various particle shapes [12, 13] and particle dynamics simulations of non-spherical particles [14], are emerging as powerful tools for gaining deeper insights into shape-dependent effects. These studies pave the way for the future design of particle shapes tailored to optimize key properties, including strength, porosity, specific surface area, and flowability for applications in various industries [15, 16].

A fundamental characteristic of non-spherical particle shapes is their ability to enhance interlocking and arching effects within a granular assembly, leading to increased shear strength [7, 10, 16, 17]. For instance, agglomerates of hexapods can exhibit exceptionally high shear strength when the friction coefficient between particles is large [4]. Assemblies of faceted particles, such as polyhedra, experience rotational constraints at face–face contacts, which contribute to higher shear strength and distinct microstructural features, including locally ordered structures [6, 18, 19]. Since particle rotations are influenced by both friction and shape, an important aspect of rheology lies in the interplay between the friction coefficient and particle geometry.

In this paper, we employ extensive particle dynamics simulations based on DEM to investigate the quasi-static rheology of dodecahedral particle packings in comparison with spherical packings. Our analysis covers both initially dense and loose systems across a range of friction coefficients. Properly modeling contact interactions between dodecahedra requires careful consideration of complex contact types, including face–face and face-edge interactions. We examine the structure of isotropic random close-packed and loose packings prepared by means of isotropic compaction under periodic boundary conditions. Then, we analyze the evolution of macroscopic properties such as shear strength, along with particle-scale characteristics including anisotropies and coordination numbers, during triaxial compression. Our findings highlight key microstructural features arising from the faceted geometry of dodecahedra, which contribute to their enhanced shear strength.

The paper is structured as follows: In Sect. 2, we introduce the numerical procedures used in our study. Section 3 examines the characteristics of isotropic states. The evolution of macroscopic variables during triaxial compression is analyzed in Sect. 4, followed by a detailed investigation of microstructural variables and their evolution in Sect. 5. The influence of particle shape is discussed and illustrated in Sect. 6. Finally, we summarize and discuss the key findings of this study in Sect. 7.

2 Numerical model

2.1 Simulation of polyhedral particles

The simulations were performed using the discrete element method (DEM), where polyhedral particles are treated as rigid bodies, while their contacts are modeled as compliant and governed by viscoelastic behavior [1, 20]. To smoothen the polyhedral particles, a Minkowski sum operation was applied with a small-radius sphere R_m [21]. This transformation replaces sharp edges with thin cylindrical elements and vertices with small spherical elements, ensuring a more realistic representation of particle interactions. As a result, each polyhedral particle consists of three subelements: (1) vertices, modeled as small spheres of radius R_m; (2) edges, represented as cylinders of radius R_m connecting two vertices; and (3) faces, treated as planes of thickness $2R_m$ that connect at least three vertices.

A key advantage of this transformation is that contacts between two polyhedra can be efficiently tracked through the interactions of their subelements, resulting in six distinct contact types: vertex–face, edge–edge, vertex–edge, vertex–vertex, edge–face, and face–face interactions. These contact types impose unilateral constraints of varying complexity. The vertex–face, vertex–edge, vertex–vertex, and edge–edge interactions involve a single contact point and can be treated similarly to contacts between spherical particles. These *simple* contacts correspond to a single unilateral constraint, as illustrated in Fig. 1a and b. In contrast, face–face interactions involve contact over a plane, requiring at least three contact points to define. Consequently, a face–face contact is equivalent to three

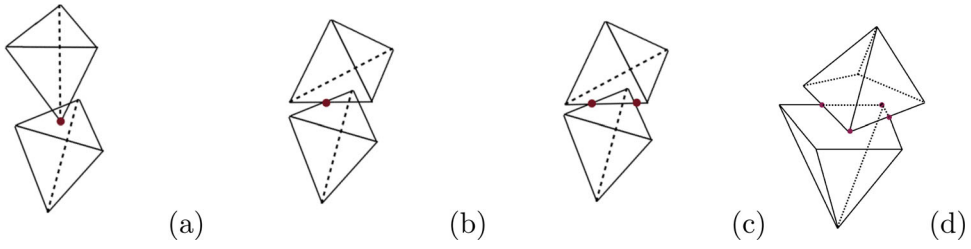

Fig. 1 Different types of contacts between two polyhedra: simple contact (**a** and **b**), double contact (**c**), and triple contact (**d**)

independent unilateral constraints [19, 22, 23]. While the actual number of contact points may exceed three, depending on the number of intersecting edges (as shown in Fig. 1d), the number of independent constraints remains limited to three due to the rigidity of the particles. Similarly, edge–face interactions require two contact points, as depicted in Fig. 1c. For this reason, the face–face and face-edge contacts are *multiple* contacts in essence and they will be respectively referred to as "double" and "triple" contacts.

At each individual contact point, either a linear or nonlinear force law is applied. For smooth particle surfaces with well-defined curvatures at the contact point, the Hertzian contact law is typically used. However, given the faceted nature of the particles in this study, we employed a linear elastic model, which is equivalent to a unilateral linear spring acting at the contact point. To incorporate contact inelasticity, a viscous damping term is added to the normal elastic repulsion force. Let $\vec{n}$ and $\vec{t}$ denote the normal and tangential unit vectors at a contact point c between particles i and j. The contact force $\vec{f} = f_n\vec{n} + f_t\vec{t}$ exerted by particle j on particle i is expressed as a function of the normal overlap δ_n and the cumulative tangential displacement $\vec{\delta}_t$.

The normal force law is defined as follows [20, 24]:

$$f_n = \begin{cases} 0, & \tilde{f}_n \le 0, \\ \tilde{f}_n, & \tilde{f}_n > 0, \end{cases} \tag{1}$$

where $\tilde{f}_n = k_n\delta_n - 2a\sqrt{k_n m}\dot{\delta}_n$. Here, k_n is the normal stiffness, δ_n represents the normal overlap (with $\delta_n > 0$ indicating particle overlap), $\dot{\delta}_n$ is the relative normal velocity, m is the reduced mass of the two contacting particles, and a is a dimensionless damping parameter ranging from 0 (fully elastic contact) to 1 (fully inelastic contact). In binary collisions, the normal restitution coefficient decreases as a increases [25, 26]. Energy dissipation in dense granular flows is a collective multi-contact process involving elastic wave propagation throughout the system. In DEM simulations, low-frequency vibration modes tend to decay slowly. To counteract this, it is common practice to enhance contact dissipation by setting the restitution coefficient close to zero (i.e., a near 1). In our simulations, we adopted a restitution coefficient of 0.001 to ensure efficient damping.

The tangential force f_t follows the Coulomb friction law:

$$f_t = \min\{|k_t\vec{\delta}_t|,\ \ \mu_s f_n\}, \tag{2}$$

where k_t is the tangential stiffness, δ_t is the cumulative tangential displacement, and μ_s is the interparticle friction coefficient. The tangential force direction $\vec{t}$ is determined by the relative motion at the contact: it opposes the relative elastic displacement $\vec{\delta}_t$ when below the Coulomb threshold, and the relative tangential velocity $\vec{v}_t$ when the threshold is reached.

2.2 Sample preparation

We generated various packings of dodecahedra and spheres, each consisting of 8000 monodisperse particles confined within a three-periodic cubic cell, allowing independent control of force or displacement in each direction [27–29]. The initial state was a gas of particles, which was subjected to isotropic compression by applying a constant isotropic stress σ_0. Gravity g and the interparticle friction coefficient μ_s were set to zero, ensuring the formation of densest isotropic samples corresponding to random close packing (RCP). The resulting packing fractions were $\Phi \simeq 0.648$ for dodecahedral particles and $\Phi \simeq 0.637$ for spherical particles.

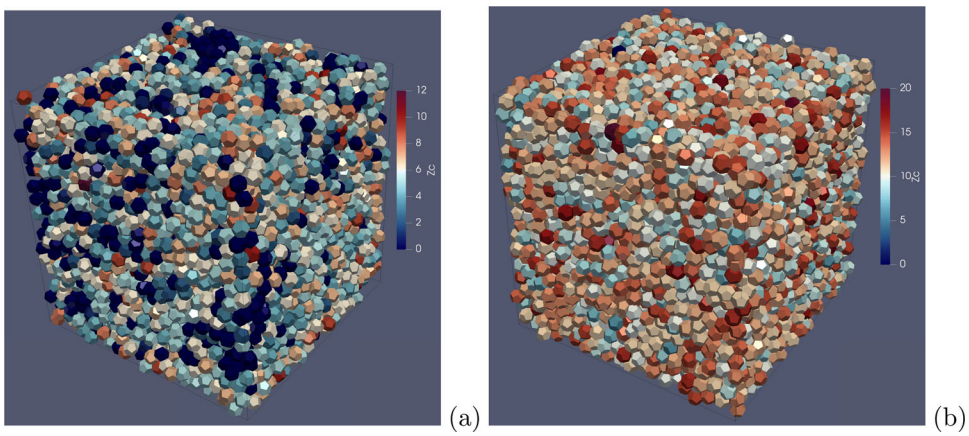

(a) (b)

Fig. 2 A snapshot of **a** loose, and **b** dense dodecahedral particle packings at the end of isotropic compaction under three-periodic boundary conditions. The friction coefficient is $\mu_s = 0.4$ in **a** and 0 in **b**. The color is proportional to the constraint number of each particle with a maximum of 12 in **a** and 20 in **b**

We also generated loose packings of spheres and dodecahedra by introducing interparticle friction during isotropic compaction. Four different values of the friction coefficient μ_s were used, ranging from 0.1 to 0.4. As expected, the resulting packings exhibited lower packing fractions (Φ) compared to RCP. In the second step, "rattlers"—particles with fewer than two contacts—were identified and removed [30–32]. Since the number of rattlers increases with μ_s, the total number of particles in the loose packings decreased accordingly.

Figure 2 presents snapshots of loose and dense polyhedral particle packings for $\mu_s = 0.4$ at the end of isotropic compaction. It is worth noting that the scales are slightly different, as the number of point contacts per particle in the dense state can reach values as high as 20, whereas in the loose state, it typically remains below 12. Similarly, as expected, the number of rattlers—particles with no contact—is significantly higher in the loose state ($\simeq 0.16$) compared to the dense state ($\simeq 0.03$). These rattlers are more easily observable in the dense state in Fig. 2a.

2.3 Triaxial compression

The isotropic dense and loose packings of spheres and dodecahedra were sheared by triaxial compression with $\mu_s = 0$ and the four nonzero values of the friction coefficient μ_s. The compression was applied along the z-axis by imposing a small constant strain rate $\dot{\varepsilon}_{zz}$ while maintaining a constant stress in the lateral directions, $\sigma_{xx} = \sigma_{yy} = \sigma_0$ (Fig. 3). Since we are interested in quasistatic behavior, the shear rate was set to a sufficiently low value to ensure negligible inertial effects. This condition can be expressed in terms of the inertia number I, defined as [33]:

$$I = \dot{\varepsilon}_{zz} d \sqrt{\frac{\rho}{\sigma_0}}, \tag{3}$$

where ρ is the particle density and d is the mean particle diameter. In our simulations, we imposed the condition $I \simeq 10^{-3}$ to remain within the quasistatic regime, following previous studies [14, 34]. As we shall see below, even at such low values of I, the particle inertia slightly affect the values of the packing fraction and coordination number. During compression, the packing evolves from its initially isotropic state towards a steady compression state in which the packing fraction Φ, the stress state and microstructural variables remain constant. We will refer to this state as the "residual state" or "critical state" [35–39].

3 Isotropic states

In this section, we analyze the properties of the final equilibrium states reached after isotropic compaction for different values of the friction coefficient. Key characteristics of isostatic states include the packing fraction Φ, the fraction P_0 of floating particles (rattlers)—defined as particles with no contacts—the coordination numbers, and the statistical distributions of local coordination numbers. The evolution of these parameters during triaxial compression will be examined in the following sections.

Figure 4 presents the packing fraction Φ for initially loose and dense packings of spheres and dodecahedra, along with the packing fraction in the residual state at the end of triaxial compression. Unlike the initial states,

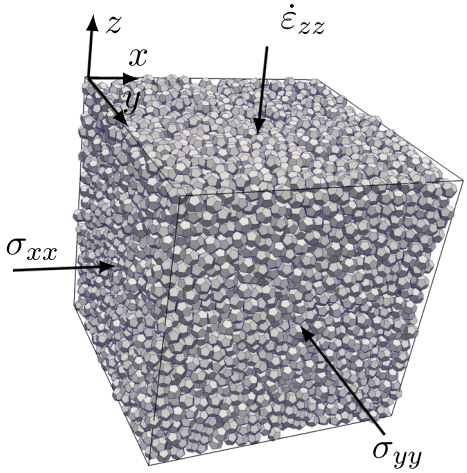

Fig. 3 A snapshot of a packing of dodecahedral particles with three-periodic boundary conditions and subjected to triaxial compression

the residual state is not isotropic, as we will see. The data show that Φ in the isotropic state of dodecahedra is slightly higher than that of spheres, indicating a stronger interlocking effect between dodecahedral particles. However, loose packings of dodecahedra exhibit lower Φ values compared to spherical particles due to the influence of face–face and face–edge contacts. As a result, the packing fraction of dodecahedral particles spans a wider range between the dense and loose limits. In initially dense packings, Φ remains unchanged with respect to μ_s since these packings were compacted under zero friction, reaching the highest random close packing fraction. Friction is introduced only before the start of triaxial compression, without affecting the initial microstructure. In contrast, loose packings were prepared with nonzero friction, as described in the previous section, leading to a decrease in Φ with increasing μ_s. A similar trend is observed in the residual state for both dodecahedra and spheres. Regardless of μ_s, the packing fraction in the residual state remains between its values in the loose and dense packings.

It is also worth examining the isotropic and residual values of Φ for the frictionless case ($\mu_s = 0$). Previous studies have shown that frictionless granular materials composed of spheres exhibit no dilatancy, despite possessing a finite shear strength [40]. As shown in Fig. 4, the residual value of Φ ($\simeq 0.631$) in our frictionless sphere packings is only slightly below its value ($\simeq 0.637$) in the initial isotropic state. However, this small dilation can be attributed to inertial effects. In fact, as demonstrated in Ref. [40], the residual value of Φ is influenced by particle inertia even at inertial numbers as low as $I = 10^{-3}$. Therefore, the small dilation observed in our simulations does not mean a nonzero Reynolds dilatancy, which by definition arises only from particle rearrangements, but rather stems from inertial contributions. Interestingly, Fig. 4 also shows that frictionless dodecahedra exhibit a similarly small decrease in Φ from the initial isotropic state ($\simeq 0.648$) to the residual state ($\simeq 0.642$). This minimal dilation, as in the case of spheres, can also be attributed to particle inertia. The absence of dilatancy in a sheared polyhedral packing is somewhat counterintuitive, as the rotation of nonspherical particles generally implies a local increase in free volume. However, it confirms the intuitive picture that, regardless of particle shape, a slowly-sheared packing of frictionless particles remains in a state of maximum compactness, corresponding to its minimum potential energy under the action of a confining pressure.

Figure 5 shows the proportion P_0 of rattlers as a function of μ_s. For both spheres and dodecahedra, P_0 increases rapidly with μ_s, with a steeper rise in dodecahedral packings than in spherical ones. At $\mu_s = 0.4$, more than 15% of the particles are rattlers, highlighting the significant role of arching in the microstructure of polyhedral particle packings. Here, "arching" refers to the formation of local arch-like structures that concentrate forces on the particles surrounding the rattlers. During compression, particles may transition into rattlers due to continuous microstructural rearrangements, contact redistributions, and the evolution of force chains.

Due to steric exclusions, the granular microstructure exhibits significant disorder at the particle scale. In the quasi-static regime, where mechanical interactions are governed by contact and friction, the structural organization

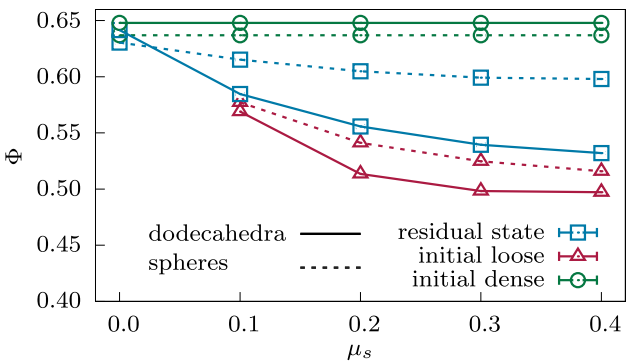

Fig. 4 Packing fraction Φ in loose and dense packings of dodecahedra and spheres together with the steady values of Φ at critical state as a function of the friction coefficient μ_s

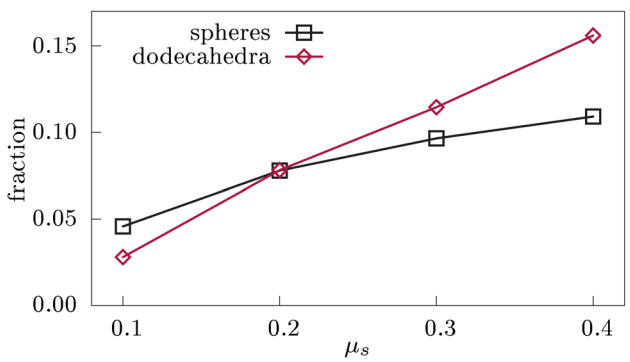

Fig. 5 Fraction of the rattlers (floating particles) for the isotropically compressed packings of spheres and dodecahedra at the end of isotropic compaction with frictional particles as a function of the interparticle friction coefficient μ_s

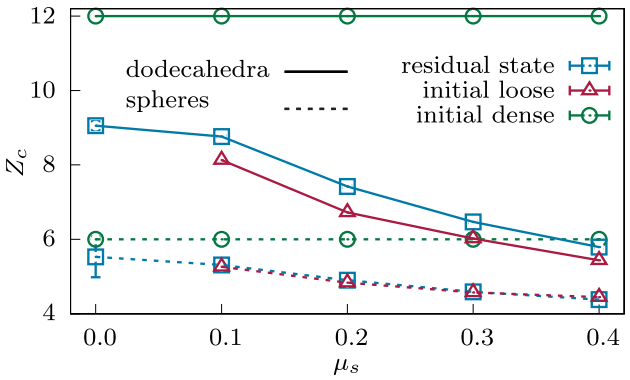

Fig. 6 Constraint number Z_c in loose and dense packings of dodecahedra and spheres, along with the values of Z_c in the residual state, as a function of the friction coefficient μ_s

of the material is primarily encoded in the force-bearing contact network. At the lowest order, this network is characterized by the coordination number Z, which denotes the average number of contact neighbors per particle [41, 42]. A *contact neighbor* is defined as any particle that shares at least one contact with a given particle. While Z is straightforward to define for spherical particles, its interpretation becomes more nuanced for polyhedral particles due to the diversity of contact types. As discussed in Ref. [6], in addition to Z, we introduce the *constraint number*, given by

$$Z_c = \frac{2(N_s + 2N_d + 3N_t)}{N_p - N_r}, \tag{4}$$

where N_s, N_d, and N_t denote the number of simple, double, and triple contacts, respectively, while N_p and N_r represent the total number of particles and rattlers. For spherical particles, Z_c coincides with Z. However, for polyhedral particles, Z_c always exceeds Z, and their ratio, Z_c/Z—referred to as the *valence number*—quantifies the average number of constraints per contact.

Figure 6 shows the constraint number Z_c as a function of μ_s for all packings of spherical and dodecahedral particles, both in their initial and residual states. Since the dense packings were generated with zero friction, they are expected to be isostatic, meaning their connectivity is constrained by the condition that the average number of normal forces per particle, $Z_c/2$, matches the number of degrees of freedom. For spheres, for which rotational degrees of freedom are immaterial due to the absence of friction forces, this number is 3, whereas for polyhedral particles, which can both Translate and rotate under the action of normal forces, it is 6. Consequently, the isostatic condition implies $Z_c = 6$ for sphere packings and $Z_c = 12$ for dodecahedral packings. Indeed, we observe a sharp transition in dense packings, where Z_c increases from approximately 6 in spherical packings to about 12 in polyhedral packings. For loose spherical packings, the values of Z_c in the initial and residual states remain nearly unchanged. However, in the residual state, Z_c falls below 6 for spherical particles and below 12 for dodecahedral particles, indicating a reduction in connectivity due to frictional effects. Furthermore, Z_c systematically decreases with increasing μ_s in both spherical and dodecahedral packings. This reflects the fact that higher friction enables a stable contact network with fewer constraints. The theoretical lower bound for an isostatic frictional packing is $Z_c = 4$, as each contact involves three force components—one normal force and two tangential frictional forces—leading to $3Z_c/2$ forces per particle. Setting this equal to the six degrees of freedom yields $Z_c = 4$. The decreasing trend observed in Fig. 6 suggests that as μ_s increases, Z_c gradually approaches

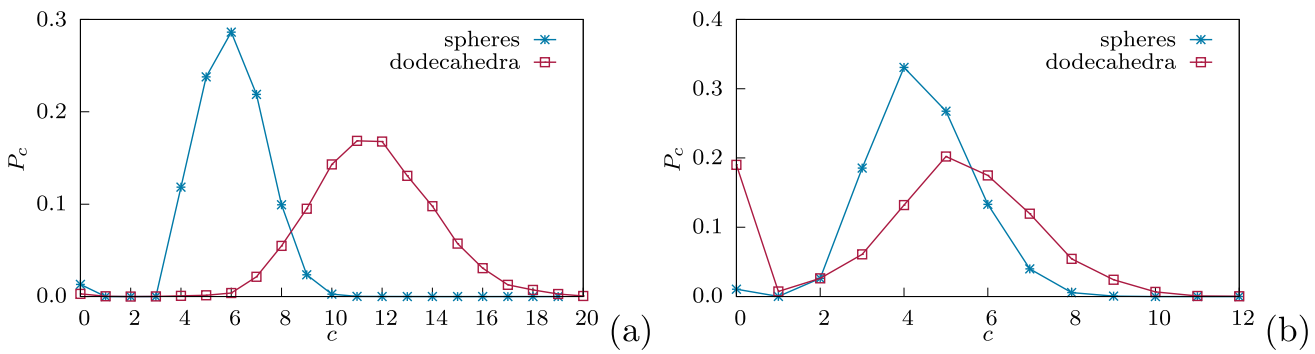

Fig. 7 The proportion P_c of particles with exactly c constraints in the dense (**a**) and loose (**b**) states for $\mu_s = 0.4$

this limit. We also note that, for both spheres and dodecahedra, the value of Z_c at $\mu_s = 0$ is slightly lower in the residual state as compared with the initial state. This decrease of Z_c aligns with the previously mentioned lower value of Φ in the residual state of frictionless particles due to small inertial effects.

Figure 7 presents the proportions P_c of particles with exactly c constraints in dense isotropic packings of spherical and dodecahedral particles obtained with $\mu_s = 0$, as well as in loose isotropic packings obtained with $\mu_s = 0.4$. In dense dodecahedral packings, P_c spans values from 4 to 20, with a peak at $c = 12$. The absence of dodecahedra with $c < 4$ indicates that their mechanical stability requires at least one face–face contact—which provides three constraints—and one simple contact or two double contacts, each contributing two constraints. For spherical particles, the peak occurs at $c = 6$, with P_c ranging from 3 to 10. The fraction P_0 of rattlers is nearly zero in both cases since they were removed in the initial preparation step, as described in the previous section. In loose packings of both spheres and dodecahedra, the distributions shift toward lower values of c, accompanied by a significant increase in P_0, consistent with Fig. 5. For spherical particles, the peak at $c = 4$ corresponds to the isostatic limit, even though the average Z_c remains above 4 due to the long tail of the distribution extending to higher values of c. For dodecahedral particles, the peak occurs at $c = 5$, much closer to the isostatic limit of $c = 4$ than in their dense counterparts.

4 Macroscopic behavior

In this section, we analyze the evolution of stress and strain in loose and dense packings during triaxial compression, considering the influence of particle shape and friction coefficient. To evaluate the stress tensor, we first compute the tensorial moment $\mathbf{M}^i$ for each particle i, defined as [43]:

$$M^i_{\alpha\beta} = \sum_{c\in i} f^c_\alpha r^c_\beta, \tag{5}$$

where f^c_α is the α component of the force exerted on particle i at contact c, and r^c_β is the β component of the position vector of the same contact. The summation runs over all contact neighbors of particle i (denoted as $c \in i$). The average stress tensor $\boldsymbol{\sigma}$ within the volume V of the granular assembly is given by the sum of the tensorial moments of individual particles, normalized by volume:

$$\sigma_{\alpha\beta} = \frac{1}{V}\sum_{i\in V} M^i_{\alpha\beta} = \frac{1}{V}\sum_{c\in V} f^c_\alpha \ell^c_\beta = n_c\langle f_\alpha \ell_\beta\rangle, \tag{6}$$

where ℓ^c_β is the β component of the branch vector connecting the centers of two contacting particles and n_c is the number density of contacts, i.e. the number of contacts per unit volume. Note that the first summation runs over all particles, whereas the second summation accounts for contacts, ensuring that each contact is counted only once.

Due to the symmetry of triaxial compression, the principal stresses and strain rates align with the three spatial directions. Let σ_1 and ε_1 represent the principal stress and strain values along the z-direction, while $\sigma_2 = \sigma_3$ and $\varepsilon_2 \simeq \varepsilon_3$ denote the values along the x- and y-directions, respectively. The mean stress p and the stress deviator q

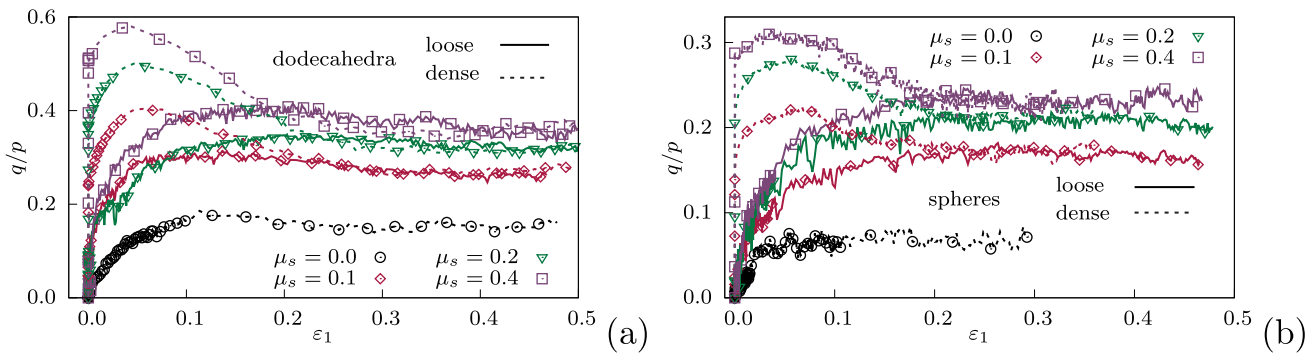

Fig. 8 Stress ratio q/p as a function of axial strain ε_1 for loose and dense packings of dodecahedra (**a**) and spheres (**b**), with four values of the friction coefficient μ_s. Dashed lines represent dense packings, while solid lines correspond to loose packings. For clarity, only a selection of data points is displayed

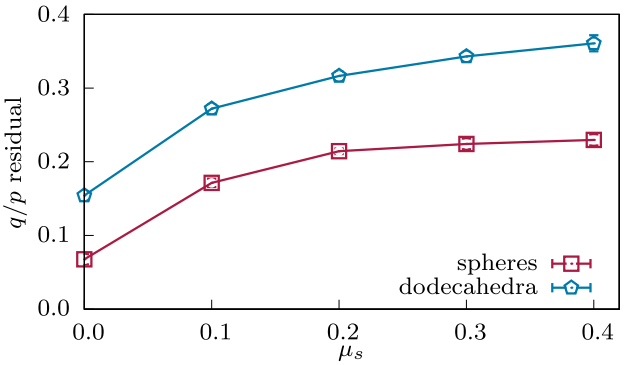

Fig. 9 Residual stress ratio q/p as a function of friction coefficient μ_s for dodecahedral and spherical particle packings

are defined as:

$$p = \frac{\sigma_1 + 2\sigma_3}{3}, \quad q = \frac{\sigma_1 - \sigma_3}{3}. \tag{7}$$

The cumulative shear strain ε_q is given by:

$$\varepsilon_q = \varepsilon_1 - \varepsilon_3. \tag{8}$$

Since the system lacks an intrinsic stress scale, the stress state is characterized by the stress ratio q/p.

Figure 8 presents the evolution of the stress ratio q/p as a function of the axial strain ε_1 for loose and dense packings of dodecahedral and spherical particles, considering different values of the friction coefficient μ_s. For dense packings, both dodecahedral and spherical, q/p rapidly increases to a peak value before decreasing and gradually stabilizing at a stress plateau, corresponding to the critical or residual state, at $\sim 30\%$ axial strain. The peak stress ratio increases with μ_s while the corresponding strain ε_1 slightly decreases. In the case of loose packings, q/p increases monotonically toward the same critical value as in dense packings, without exhibiting a peak. This is the well-known behavior in soil mechanics, where the critical-state shear strength is independent of the initial state [35, 36, 44]. It is also remarkable that the stress ratio does not vanish for $\mu_s = 0$, indicating that the shear strength of granular materials has both collisional and frictional origins [45]. Furthermore, for all values of ε_1, including both peak and residual states, the stress ratio q/p is consistently higher in dodecahedral particle packings than in spherical ones. This is an expected consequence of polyhedral particle geometry, as face–face contacts contribute to enhanced mechanical stability. This point will be analyzed in more detail below in terms of the fabric and force anisotropies.

It is important to note that, due to the application of three-periodic boundary conditions, no persistent shear bands develop in these simulations. As a result, the mechanical response—in terms of the evolution of shear stress and packing fraction—becomes an intrinsic property of the material itself. It is well known that dense granular materials subjected to conventional triaxial compression tests tend to become unstable near the stress peak, leading to the formation of shear bands. In such cases, the observed behavior is no longer purely inherent to the material; it is influenced, at least in part, by the boundary conditions. In particular, once strain localizes within the shear bands, the volume changes measured at the sample scale reflect only those occurring inside the localized zones. Simulations with fully periodic boundary conditions make it possible to capture the intrinsic material behavior by avoiding the onset of shear localization. Once this inherent response is characterized using such boundary conditions, the stability of the system and the onset of shear banding can then be assessed through bifurcation analysis.

Figure 9 displays the residual stress ratio q/p as a function of the friction coefficient μ_s for both dodecahedral and spherical particles. As previously stated, the residual value of q/p at $\mu_s = 0$ is nonzero as a result of dissipation due to inelastic collisions between particles. As μ_s increases, q/p increases rapidly but levels off at a constant value around $\mu_s = 0.4$. This saturation occurs because higher friction enhances the energy cost at sliding contacts, promoting rolling instead and leading to a reduction in the number of contacts. This nonlinear dependence of q/p on μ_s closely resembles the behavior of the packing fraction Φ, as seen in Fig. 4. Beyond $\mu_s = 0.4$, further increase of friction has no effect on the residual state, neither on q/p nor on Φ.

The evolution of the packing fraction Φ as a function of axial strain ε_1 is presented in Fig. 10 for both dodecahedral and spherical particle packings. As previously discussed, in dense packings, a unique random close-packed configuration—generated via isotropic compaction with zero friction—is sheared under different values of the friction coefficient μ_s. Consequently, Φ gradually decreases from a common initial value to distinct residual values depending on μ_s. This trend occurs also in the case of frictionless particles, but the overall variation of Φ is small

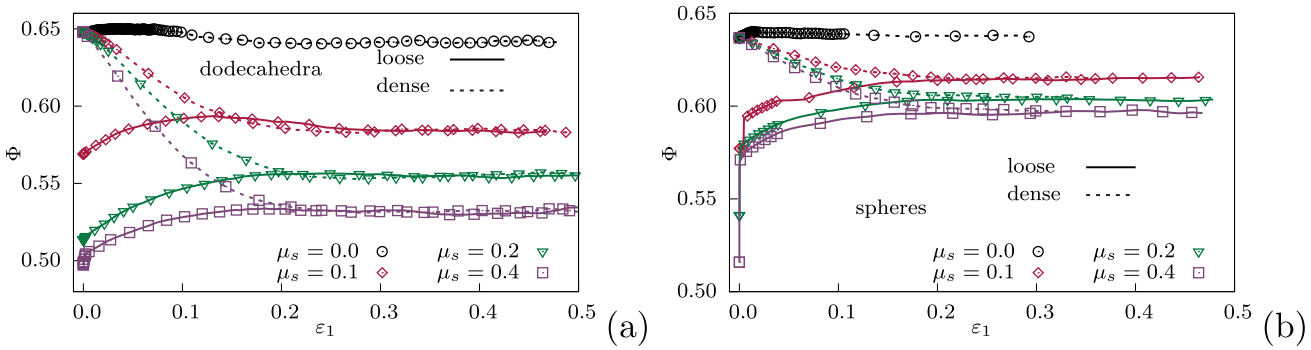

Fig. 10 Packing fraction Φ as a function of axial strain ε_1 for loose and dense packings of dodecahedra (**a**) and spheres (**b**) with four values of the friction coefficient μ_s. Dashed lines represent dense packings, while solid lines correspond to loose packings. For clarity, only a selection of data points is displayed

and may be attributed to reminiscent inertial effects. For loose packings, Φ initially exhibits a pronounced increase as the system undergoes contraction due to its low initial density. This is followed by a slower rise, eventually converging toward the same residual value as in dense packings. For any given μ_s, the packing fraction Φ remains consistently lower in dodecahedral particle packings compared to spherical ones. Thus, the residual state for each friction coefficient μ_s is characterized by well-defined values of both the residual stress ratio and the packing fraction.

5 Evolution of microstructure

We previously analyzed the constraint number Z_c, identified as the lowest-order parameter of a granular texture, in isotropic states. In this section, we focus on its evolution in packings of dodecahedral and spherical particles and the influence of the friction coefficient μ_s. Granular textures inherently exhibit also various degrees of anisotropy due to the relative motions of particles during shear. These rearrangements lead to the formation of contacts along the compression direction and the loss of contacts along the extension direction. We will examine the parameters characterizing this anisotropy and their evolution during triaxial compression.

5.1 Constraint number

Figure 11 shows the evolution of the constraint number Z_c during triaxial compression for both loose and dense packings of dodecahedral and spherical particles. In loose packings, Z_c gradually increases until it stabilizes at its final value in the residual state. In contrast, dense packings exhibit a sharp decline in Z_c, dropping from 12 for dodecahedra and 6 for spheres to the same residual value as in loose packings. This Transition occurs within less than 4% axial strain—significantly faster than the 30% strain required for Φ and q/p to reach stability. The abrupt decrease of Z_c in dense packings highlights their ability to lose contacts along the extension direction without compromising stability. As deformation progresses, the system reaches a dynamic equilibrium where contact gains and losses balance, leading to a constant number of contacts.

This evolution is different in the case $\mu_s = 0$ where we observe a plateau just after the initial decrease, followed by a fast decrease around $\varepsilon \simeq 0.1$. The plateau is much more evident in the case of dodecahedra. The presence of this plateau for both spherical and dodecahedral particles indicates the stability of the initial granular structure generated by isotropic compaction in transition to an anisotropic structure. For dodecahedra, the plateau is more pronounced as a result of the relative stability of the double and triple contacts. As we shall see in Sect. 5.2, the maximum anisotropy of frictionless samples is reached at $\varepsilon \simeq 0.1$. This means that the evolution of the microstructure of frictionless samples occurs in two distinct regimes: (1) From $\varepsilon \simeq 0.01$ to $\varepsilon \simeq 0.1$, Z_c remains constant but the fabric anisotropy increases, and (2) beyond $\varepsilon \simeq 0.1$, the anisotropy remains constant and Z_c declines.

The rapid stabilization of Z_c for frictional particles does not imply that the contact network ceases to evolve. Instead, two key microstructural processes continue to influence the system:

1. Transitions between simple, double, and triple contacts, which redistribute constraints within the network.
2. The evolution of microstructural anisotropy, which plays a crucial role in the overall mechanical response of the packing.

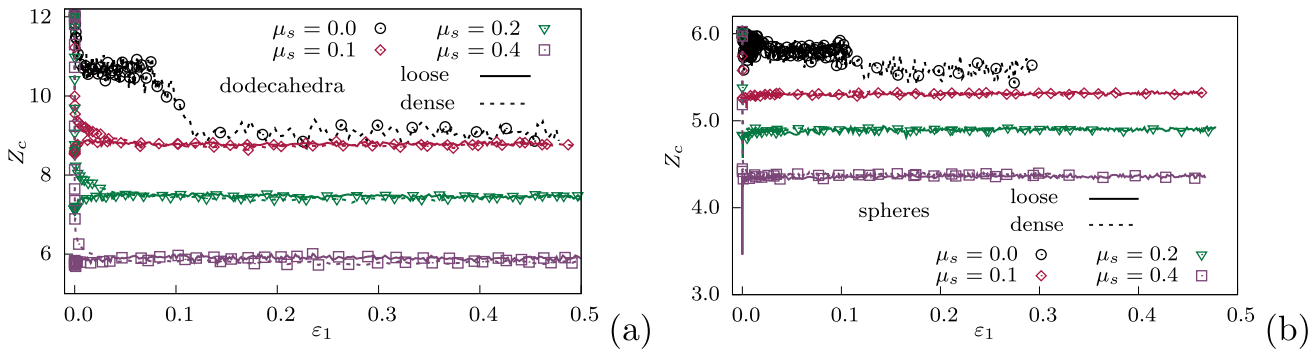

Fig. 11 Evolution of the constraint number Z_c as a function of axial strain ε_1 for both loose and dense packings of dodecahedral and spherical particles, considering four different values of the friction coefficient μ_s. Dashed lines represent dense packings, while solid lines correspond to loose packings. For clarity, only a selection of data points is displayed

These aspects will be discussed in Sect. 6.

5.2 Shear-induced anisotropy

The anisotropic structure can be quantitatively described using the fabric tensor $\mathbf{F}$, constructed from contact normals $\vec{n}$, or alternatively through the probability density function $P(\vec{n})$, which represents the likelihood of a contact normal being oriented along $\vec{n}$ [46, 47]. For polyhedral particles, anisotropy can be analyzed using either contact normals, which corresponds to the contact frame $(\vec{n},\ \vec{t},\ \vec{s})$, or the orientations $\vec{n'}$ of the branch vectors $\vec{\ell}$ connecting particle centers, corresponding to the branch vector frame $(\vec{n'},\ \vec{t'},\ \vec{s'})$. Figure 12 illustrates these two frames. In the case of spherical particles, the contact and branch vector frames coincide. For convex particles, they remain parallel on average. Indeed, our analysis confirms that in our samples, we have $\langle \vec{n} \cdot \vec{n'} \rangle \simeq 1$. Based on this observation, we will restrict our analysis to the branch vector frame $(\vec{n'},\ \vec{t'},\ \vec{s'})$.

In spherical coordinates, the unit vector $\vec{n'}$ along the branch vector can be expressed using the azimuthal angle ϕ and the latitude angle θ. The general parametrization is given by:

$$\begin{cases} \vec{n'} = (\cos\theta,\ \sin\theta\cos\phi,\ \sin\theta\sin\phi), \\ \vec{t'} = (-\sin\theta,\ \cos\theta\cos\phi,\ \cos\theta\sin\phi), \\ \vec{s'} = (0,\ -\sin\phi,\ \cos\phi), \end{cases} \tag{9}$$

where the angles are defined within the ranges $\theta \in [0,\ \pi]$ and $\phi \in [0,\ 2\pi]$. Under the axi-symmetric conditions of triaxial compression, the probability density function $P(\vec{n'})$ remains independent of the angle ϕ. Consequently, within a second-order harmonic approximation, it can be expressed as:

$$P(\vec{n'}) = P(\Omega) = P_\theta(\theta) = \frac{1}{4\pi}\left[1 + a_c(3\cos^2\theta - 1)\right], \tag{10}$$

where Ω represents the solid angle defining the orientation of $\vec{n'}$, with $d\Omega = \sin\theta d\theta d\phi$, and a_c is the parameter characterizing the second-order contact orientation anisotropy.

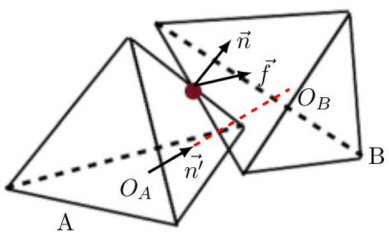

Fig. 12 Geometry of a contact between two polyhedra. $\vec{n}$ is the unit normal vector at the contact point, whereas $\vec{n'}$ is the unit normal vector along the branch vector joining the centers O_A and O_B of the two particles

In practice, the parameter a_c can be conveniently derived from the fabric tensor $\mathbf{F}$, which is defined as:

$$F_{ij} = \int_\Omega n'_i n'_j P(\Omega) d\Omega = \frac{1}{N_c} \sum_{c \in V} n'c_i n'c_j, \tag{11}$$

where i and j represent the components in a reference frame, and N_c is the total number of contacts within the control volume V. By combining Eqs. (9), (10), and (11), the eigenvalues of the fabric tensor are obtained as follows:

$$\begin{cases} F_1 = \displaystyle\int_\Omega n'^2_1 P(\Omega) d\Omega = \frac{5 + 4a_c}{15}, \\ F_2 = F_3 = \displaystyle\int_\Omega n'^2_2 P(\Omega) d\Omega = \frac{5 - 2a_c}{15}. \end{cases} \tag{12}$$

From Eqs. (9), (10), and (12), the anisotropy parameter a_c can be expressed as:

$$a_c = \frac{5}{4} \langle 3 \cos^2 \theta - 1 \rangle. \tag{13}$$

The term $\langle 3 \cos^2 \theta - 1 \rangle$ quantifies the anisotropy and can be evaluated either from $P(\Omega)$ or directly from numerical data. However, a more practical approach is to compute the fabric anisotropy using the relationship [48, 49]:

$$a_c = \frac{5}{2}(F_1 - F_2). \tag{14}$$

Here, the eigenvalue F_1 corresponds to the compression axis, while the two remaining eigenvalues satisfy $F_2 = F_3 = (1 - F_1)/2$.

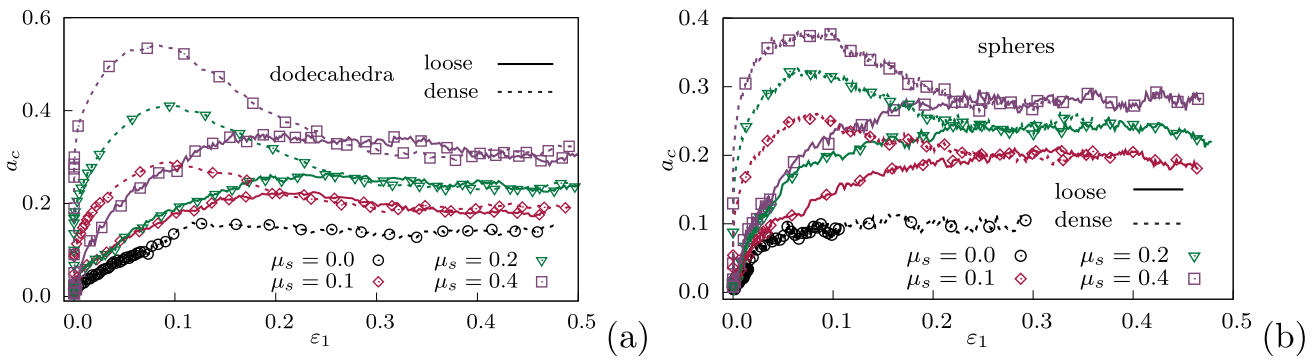

Fig. 13 Fabric anisotropy a_c as a function of axial strain ε_1 for loose and dense packings of dodecahedra (**a**) and spheres (**b**) with four values of the friction coefficient μ_s. Dashed lines represent dense packings, while solid lines correspond to loose packings. For clarity, only a selection of data points is displayed

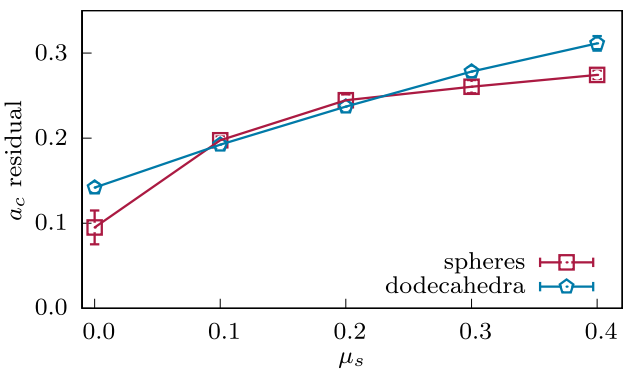

Fig. 14 Fabric anisotropy a_c in the residual state as a function of friction coefficient μ_s for dodecahedral and spherical particle packings

Figure 13 shows the evolution of the anisotropy parameter a_c during triaxial compression for both loose and dense packings of dodecahedra and spheres. Initially, fabric anisotropy increases due to the loss of contacts perpendicular to the compression axis in dense packings and the gain of new contacts along the contraction direction in loose packings. For dense packings, a_c reaches a peak state before gradually decreasing to a steady value in the residual state, where contact gains and losses become balanced. In contrast, for loose packings, a_c progressively increases until stabilizing at the residual state. Unlike dense packings, it does not exhibit a peak, as contact gain dominates throughout shear deformation. We note the nonzero value of a_c for $\mu_s = 0$, showing that a nearly isostatic packing can have an anisotropic texture. Figure 14 presents the residual anisotropy as a function of μ_s for both types of packings. The trend closely resembles that of the stress ratio q/p (see Fig. 9), with a nonzero initial value at $\mu_s = 0$ followed by an increasing trend as μ_s rises. The fabric anisotropies of spherical and dodecahedral packings in the residual state are remarkably similar up to its slightly higher value in the dodecahedra packing for $\mu_s = 0$ and $\mu_s = 0.4$.

Force anisotropies are generally characterized by analyzing the average normal and tangential contact forces, $\langle f_n \rangle(\theta)$ and $\langle f_t \rangle(\theta)$, as functions of the contact orientation θ. In the branch vector frame used in this work, we consider the contact force components $f_{n'}$ and $f_{t'}$ along and perpendicular to the branch vectors. They represent the *radial* and *ortho-radial* force components, respectively. For spheres, they coincide with normal force and tangential force, respectively. A second-order Fourier expansion (or spherical harmonics) provides a suitable approximation of these force distributions:

$$\begin{cases} \langle f_{n'} \rangle(\theta) = \langle f_{n'} \rangle \big[1 + a_n (3\cos^2\theta - 1)\big], \\ \langle f_{t'} \rangle(\theta) = \langle f_{n'} \rangle a_t \sin 2\theta, \end{cases} \tag{15}$$

where a_n and a_t denote the radial and ortho-radial anisotropies, respectively.

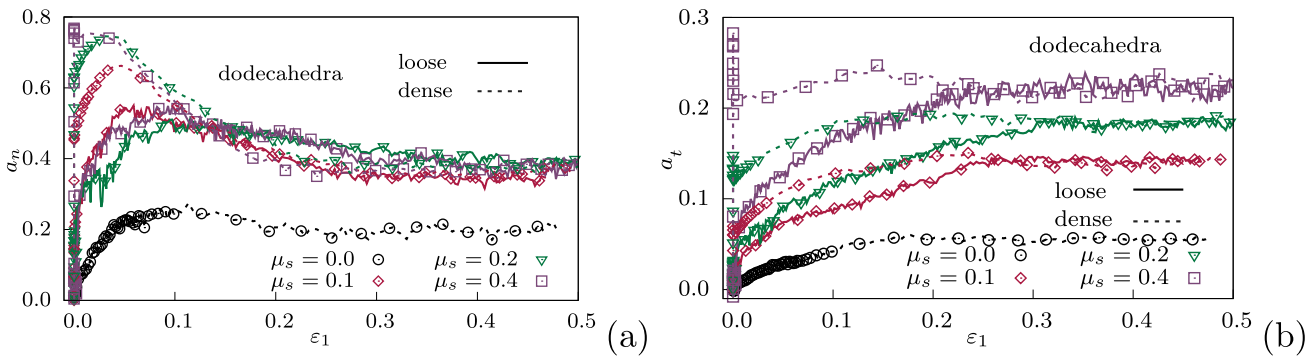

Fig. 15 Radial force anisotropy a_n (**a**) and ortho-radial force anisotropy a_t (**b**) as a function of axial strain ε_1 for loose and dense packings of dodecahedra with four values of the friction coefficient μ_s. Dashed lines represent dense packings, while solid lines correspond to loose packings. For clarity, only a selection of data points is displayed

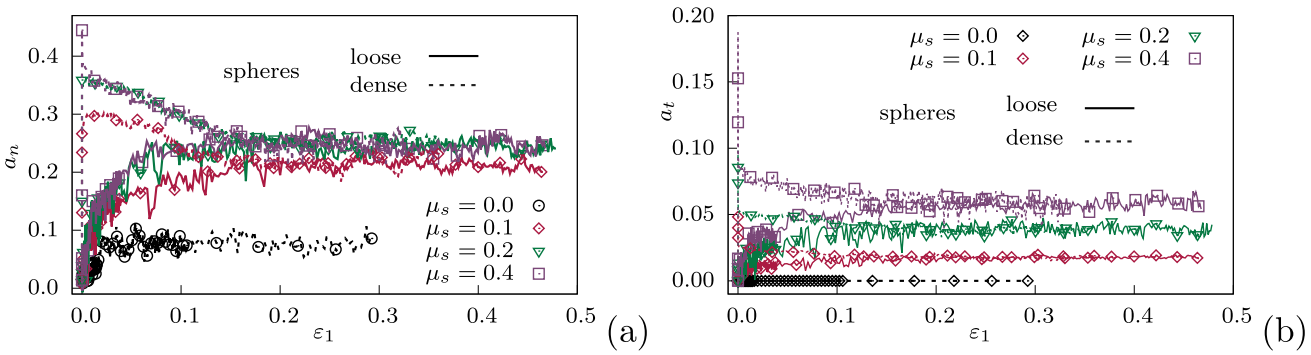

Fig. 16 Radial force anisotropy a_n (**a**) and ortho-radial force anisotropy a_t (**b**) as a function of axial strain ε_1 for loose and dense packings of spherical particles for four values of the friction coefficient μ_s. Dashed lines represent dense packings, while solid lines correspond to loose packings. For clarity, only a selection of data points is displayed

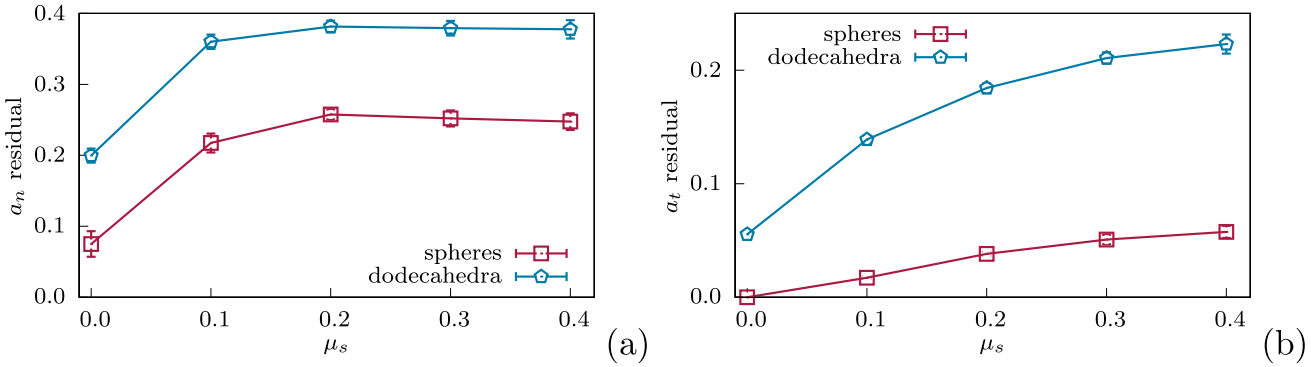

Fig. 17 Radial force anisotropy a_n (**a**) and ortho-radial force anisotropy a_t (**b**) in the residual state as a function of friction coefficient μ_s for dodecahedra and spheres

These anisotropy parameters can be computed using the force tensors [48]:

$$\begin{cases} \chi_{ij}^{n'} = \dfrac{1}{\langle f_{n'} \rangle} \displaystyle\int_\Omega \langle f_{n'} \rangle(\theta) n_i' n_j' P(\theta) d\Omega, \\ \chi_{ij}^{t'} = \dfrac{1}{\langle f_{n'} \rangle} \displaystyle\int_\Omega \langle f_{t'} \rangle(\theta) n_i' t_j' P(\theta) d\Omega. \end{cases} \tag{16}$$

From these definitions, the following relationships can be derived:

$$\begin{cases} a_n = 2.5(\chi_1^{n'} - \chi_2^{n'}) - a_c, \\ a_t = 2.5(\chi_1^{t'} - \chi_2^{t'}) - a_c, \end{cases} \tag{17}$$

where the indices 1, 2, and 3 refer to the principal values of each tensor. The triaxial symmetry of the system implies $\chi_2^{n'} = \chi_3^{n'}$ and $\chi_2^{t'} = \chi_3^{t'}$.

Figures 15 and 16 show the evolution of radial and ortho-radial force anisotropies, a_n and a_t, as functions of axial strain ε_1 for dodecahedral and spherical packings at various friction coefficients. For both particle shapes, a_n and a_t ultimately reach a unique steady-state value in the residual state, regardless of initial packing density. However, in dense packings, they exhibit a pronounced peak before stabilizing. Figure 17 presents the residual values of a_n and a_t for both packing types as a function of μ_s. The radial force anisotropy a_n remains nonzero even at $\mu_s = 0$. In contrast, for spheres, the ortho-radial force anisotropy a_t vanishes at $\mu_s = 0$, whereas for dodecahedra, it retains a small but nonzero value ($\simeq 0.05$). Both a_n and a_t increase significantly with μ_s, though the impact of friction and particle shape is more pronounced on a_t. According to Eq. (15), a_t reflects the average friction mobilization $\langle f_t \rangle / \langle f_n \rangle$ at an angle of $\pi/4$ relative to the compression axis. The markedly higher values of a_t for dodecahedra compared to spheres indicate the combined effects of both a stronger friction mobilization and the enhanced normal force component along the ortho-radial directions. The increase of a_t in dodecahedra packings compared to sphere packings represents therefore an important signature of nonspherical particle shape.

In addition to the anisotropies discussed so far, the branch vectors $\vec{\ell} = \ell \vec{n'}$ exhibit length anisotropy due to the dependence of the average length $\langle \ell \rangle$ on the orientation θ of $\vec{n'}$. This dependence can be expressed using a truncated Fourier expansion:

$$\langle \ell \rangle(\theta) = \langle \ell \rangle \left[1 + a_\ell (3 \cos^2 \theta - 1) \right], \tag{18}$$

where a_ℓ represents the branch vector length anisotropy. To compute a_ℓ, we introduce the branch length tensor:

$$\chi_{ij}^{\ell} = \frac{1}{\langle \ell \rangle} \int_\Omega \langle \ell \rangle(\theta) n_i' n_j' P(\theta) d\Omega, \tag{19}$$

from which we derive:

$$a_\ell = 2.5(\chi_1^{\ell} - \chi_2^{\ell}) - a_c. \tag{20}$$

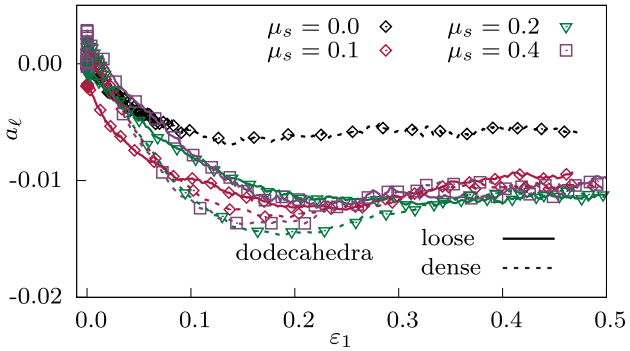

Fig. 18 Branch anisotropy a_ℓ as a function of axial strain ε_1 for loose and dense packings of dodecahedra with four values of the friction coefficient μ_s. Dashed lines represent dense packings, while solid lines correspond to loose packings. For clarity, only a selection of data points is displayed

For spherical particles, a_ℓ is zero since the system is monodisperse, and the average branch vector length remains constant at twice the particle radius. In contrast, for dodecahedral particles, ℓ varies based on their relative positions.

Figure 18 illustrates the evolution of a_ℓ as a function of axial strain for different values of μ_s. In both dense and loose packings, a_ℓ decreases from 0 to a constant value in the residual state. The negative sign indicates that the major principal direction of χ_{ij}^{ℓ} is perpendicular to the axial direction, implying shorter average branch vector lengths along the compression axis. Since the shortest branch vectors correspond to face–face contacts, the observed negative values suggest that these contacts predominantly align with the axial direction. The absolute value of a_ℓ is higher for frictional particles as compared with the frictionless case. This is consistent with the fact that friction allows for a higher variability of ℓ. Furthermore, the absolute value of a_ℓ is significantly smaller than those of a_c or a_n, and friction has little influence on its magnitude. This suggests that length anisotropy plays a relatively minor role compared to fabric and force anisotropies. However, its negative value for dodecahedra represents an interesting new feature that has no equivalent in the case of monodisperse spherical particles. A nonzero but positive value of a_ℓ was evidenced in simulations in sheared packings of polydisperse spherical particles [50].

6 Effect of particle shape

In this section, we investigate the mechanisms underlying the higher shear strength of dodecahedral packings compared to spherical ones. We first analyze the additive partition of shear stress in terms of the various anisotropies introduced in the previous section. Then, we examine the influence of double and triple contacts and their contribution to the anisotropic structure of dodecahedral packings.

6.1 Origins of shear stress

From the general expression of the stress tensor (6) and using the definitions of the fabric and force tensors, the stress ratio q/p can be expressed as a function of a_c, a_n, a_t, and a_ℓ [19, 41, 46]:

$$\frac{q}{p} \simeq \frac{2}{5}(a_c + a_n + a_t + a_\ell), \tag{21}$$

where the cross products among the anisotropy parameters have been neglected. This relation reveals the three origins of shear stress in a granular system:

1. the fabric anisotropies a_c and a_ℓ, related to the branch vector,
2. the strong force chains essentially captured by a_n,
3. friction mobilization quantified by a_t.

Equation (21) clearly shows that friction mobilization is not the only factor giving rise to the strength but that the contributions of the force chains and the contact network anisotropy can even be more important. This equation is in excellent agreement with our data for both dodecahedra and spheres as shown in Fig. 19 for $\mu_s = 0.1$. The larger value of q/p in the dodecahedral particle packing is therefore mainly due to a_n and a_t, which have larger values for dodecahedra than for spheres while a_c is only slightly affected by particle shape. The origins of the larger values of a_n and a_t were discussed in the previous section. In short, they reflect the higher stability of face–face contacts and the role of normal force components in the ortho-radial direction.

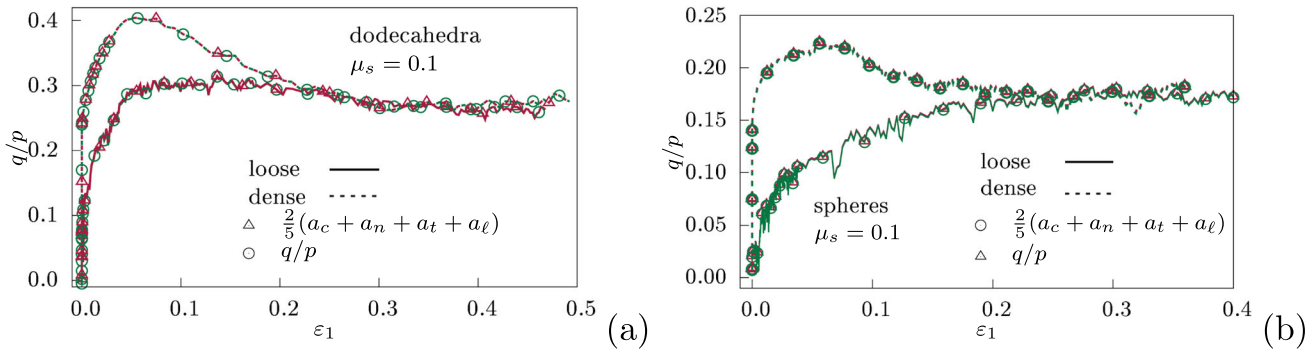

Fig. 19 Stress ratio q/p as a function of axial strain ε_1 for loose and dense packings of dodecahedra and spheres for friction coefficient $\mu_s = 0.1$ together with the analytical expression given by Eq. (21). Dashed lines represent dense packings, while solid lines correspond to loose packings. For clarity, only a selection of data points is displayed

6.2 Role of contact types

The constraint number Z_c can be analyzed by considering its contribution from different contact types. We define the partial constraint numbers Z_{c1}, Z_{c2}, and Z_{c3} for simple, double, and triple contacts, respectively, such that $Z_c = Z_{c1} + Z_{c2} + Z_{c3}$. This means that the average numbers of double and triple contacts per particle are $Z_{c2}/2$ and $Z_{c3}/3$, respectively. Figure 20 shows the evolution of Z_{c1}, Z_{c2}, and Z_{c3} as a function of ε_1 for both dense and loose packings of dodecahedra across all values of μ_s. The results indicate that all three constraint numbers decrease with increasing friction coefficient.

Except for $\mu_s = 0$, the behavior of Z_{c2} closely mirrors that of Z_c, exhibiting a sharp decrease in dense packings followed by a slight increase within 4% axial strain. However, Z_{c1} and Z_{c3} display more complex non-monotonic variations. In dense samples, Z_{c1} initially declines, reaches a minimum, and then rises again, while Z_{c3} initially drops, then increases before eventually decreasing. In loose samples, Z_{c1} decreases after an initial rise, whereas Z_{c3} gradually increases. These opposing trends result in a near-constant value of Z_c beyond 4% axial strain, suggesting that simple and triple contacts frequently transition into double contacts, while double contacts convert into either

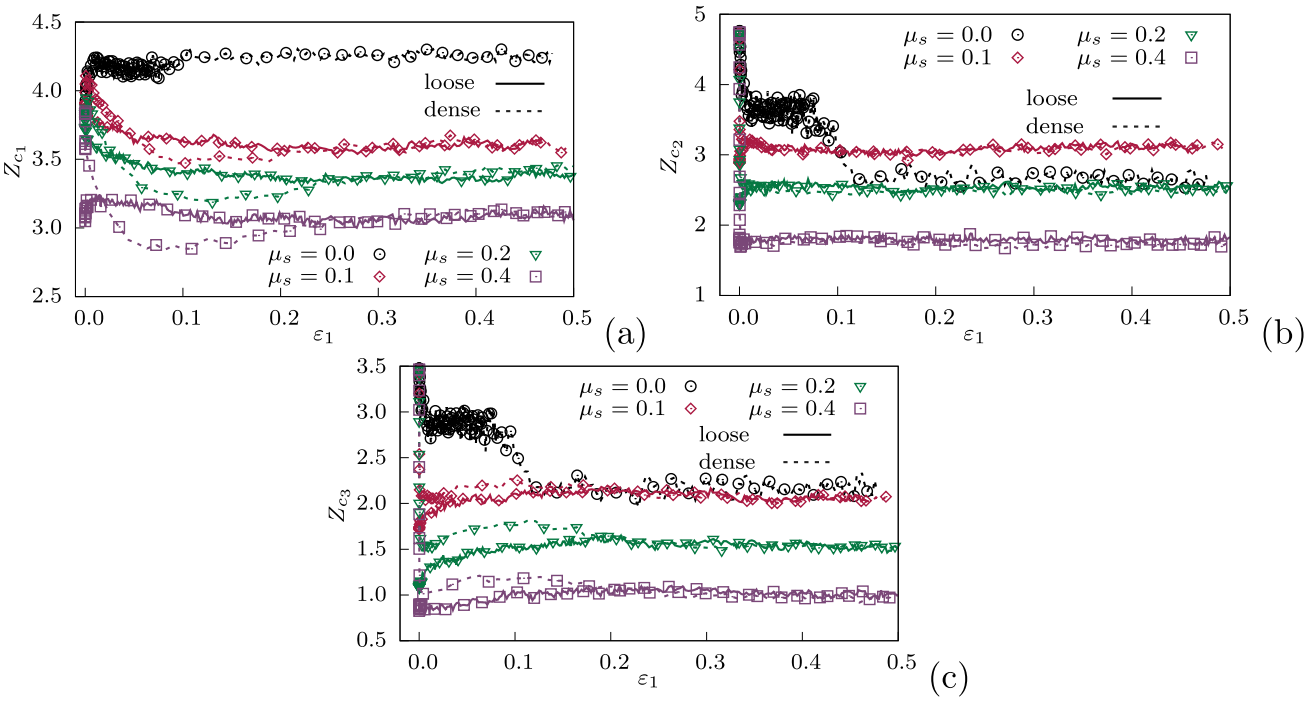

Fig. 20 Partial constraint numbers Z_{c1}, Z_{c2}, and Z_{c3} for dodecahedral and spherical particles as a function of axial strain ε_1. Dashed lines represent dense packings, while solid lines correspond to loose packings. For clarity, only a selection of data points is displayed

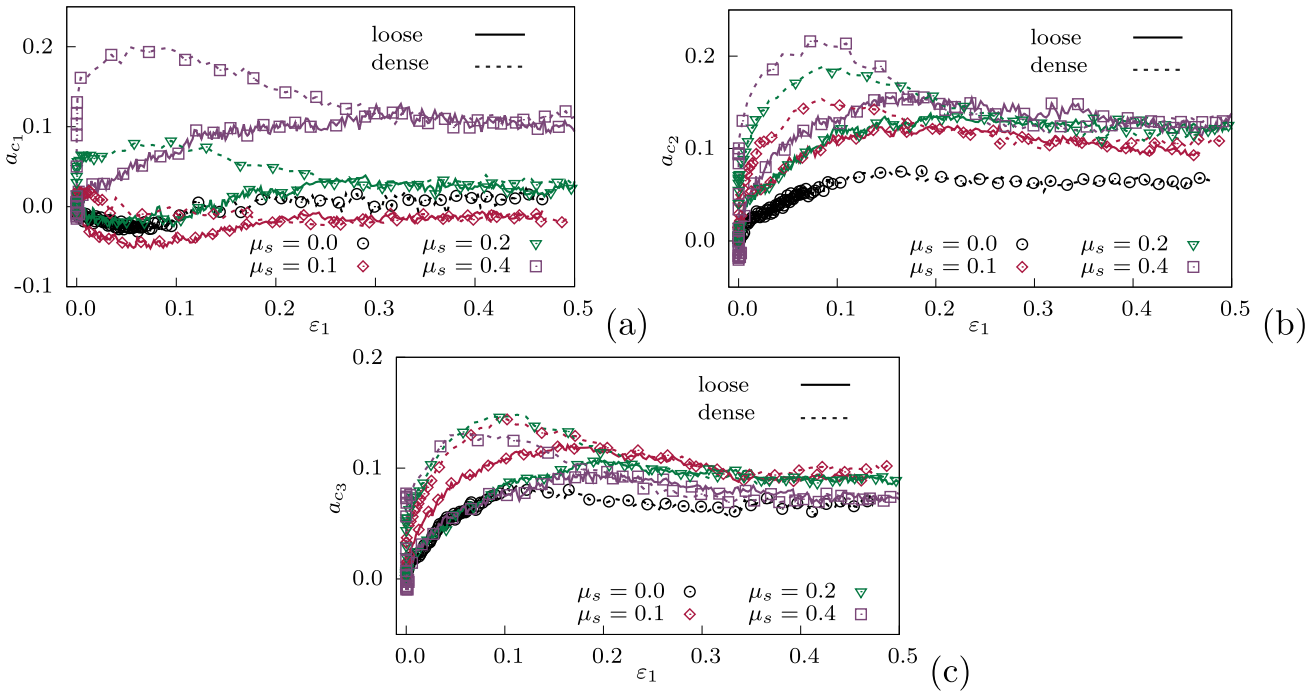

Fig. 21 Fabric anisotropies of simple contacts (**a**), double contacts (**b**), and triple contacts (**c**) as a function of axial strain ε_1 for loose and dense packings of dodecahedra for various values of the friction coefficient μ_s. Dashed lines represent dense packings, while solid lines correspond to loose packings. For clarity, only a selection of data points is displayed

simple or triple contacts. When these transitions occur at similar rates, Z_{c2} remains relatively stable, as observed in the data. These changes contribute to the stabilization of Φ and q/p, underscoring the complex interplay between contact transitions and anisotropic structural rearrangements. For all values of μ_s, simple contacts represent the largest proportion, followed by double and then triple contacts, highlighting their respective contributions to the contact network. The case of samples with $\mu_s = 0$ is slightly different. Z_{c1} increases with ε_1 to a high value ($\simeq 4.3$) whereas Z_{c2} and Z_{c3} first decline, remain constant until $\varepsilon_1 = 0.1$, and then decline again to a value respectively below and slightly above that of the case $\mu_s = 0.1$. The existence of this plateau was discussed in Sect. 5.1 for Z_c. Here, we see that even the organization of different contact types remains unchanged in this regime.

The contributions of different contact types to the fabric anisotropy can be distinguished similarly to the constraint number in dodecahedral packings. Figure 21 presents the evolution of fabric anisotropies a_{c1}, a_{c2}, and a_{c3}, corresponding to simple, double, and triple contacts, respectively, as a function of axial strain ε_1 for various values of the friction coefficient μ_s. While the general behavior resembles that of a_c, notable differences arise in the values and signs of the anisotropies. In particular, for $\mu_s = 0.1$ and $\mu_s = 0.2$, a_{c1} takes negative values, indicating that simple contacts are, on average, oriented perpendicular to the compression axis. This observation suggests that the simple contacts tend to prop the double and triple contacts oriented along the axis. Another remarkable observation is that triple contacts, despite representing a small fraction of contacts, contribute nearly one-third of the total fabric anisotropy. For instance, at $\mu_s = 0.4$, the residual anisotropies are approximately $a_{c1} \simeq 0.1$, $a_{c2} \simeq 0.12$, and $a_{c3} \simeq 0.08$. Additionally, the residual anisotropy increases with increasing μ_s for simple and double contacts, while it slightly decreases for triple contacts, leading to an almost constant sum $a_{c2} + a_{c3}$ across different friction values. Since double and triple contacts are inherently more stable than simple contacts and are associated with strong force chains, their high anisotropy is at the origin of the higher values of the corresponding force anisotropies a_n and a_t in dodecahedral particle packings as compared with sphere packings.

7 Conclusions

In this paper, we used particle dynamics simulations to investigate the influence of particle shape and friction coefficient between particles on the mechanical behavior and microstructural features of granular media, comparing spherical and dodecahedral particle packings under isotropic compaction and triaxial compression. Our findings highlight the crucial role of particle shape for the macroscopic properties such as the shear strength and packing fraction.

Our analysis confirms that dodecahedral particles exhibit a stronger interlocking, leading to a broader range of packing fraction variation. In a similar vein, the fraction of rattlers increases with friction for both dodecahedra and spheres, but more steeply for dodecahedral packings, reflecting the pronounced role of arching in polyhedral assemblies. The constraint number, which quantifies contact network connectivity by accounting for the geometrical constraints associated with face–face (triple) and face–edge (double) contacts, decreases systematically with increasing friction coefficient, approaching theoretical isostatic limits.

During triaxial compression, both dense and loose packings evolve toward a critical or residual state, erasing memory of their initial configurations. The stress ratio, defined as the ratio of stress deviator to average stress, consistently reaches higher values in dodecahedral packings than in spherical ones, confirming the reinforcement effect of face–face contacts. While this ratio increases with friction coefficient up to 0.4, it saturates beyond this threshold.

We also investigated the evolution of structural and mechanical anisotropies in granular packings of dodecahedra and spheres under triaxial compression, emphasizing the effects of contact fabric, force anisotropies, and particle shape. Our analysis revealed that the evolution of the fabric anisotropy is strongly influenced by the friction coefficient, with distinct trends for dense and loose packings. The fabric anisotropy increases initially due to contact rearrangements and stabilizes at a residual state, with dodecahedral and spherical packings exhibiting comparable values despite their differing geometries. We further examined the radial and ortho-radial force anisotropies, demonstrating that both parameters increase with friction coefficient and play a crucial role in the overall stress anisotropy. The ortho-radial anisotropy is particularly sensitive to particle shape, with dodecahedral packings exhibiting significantly higher values than spheres, even at zero friction between particles. In the latter case, the ortho-radial force anisotropy does not arise from the mobilization of friction forces—since these are absent at zero friction coefficient—but rather from the projection of normal forces onto the branch vectors. Therefore, the enhanced ortho-radial force anisotropy observed in packings of frictional dodecahedra results from a combination of friction mobilization and the geometric projection of normal forces.

Another key aspect of our study was the anisotropy of branch vector lengths. We showed that in dodecahedral packings, this anisotropy remains negative, indicating a shorter average branch length along the compression axis. This was attributed to the dominance of face–face contacts in this direction. However, its magnitude remains smaller than those of the fabric and force anisotropies. Finally, we analyzed the contributions of different contact types—simple, double, and triple—to the overall anisotropies. Triple contacts, despite their limited number, contribute disproportionately to fabric anisotropy, particularly at high values of friction coefficient. Their high stability and alignment with strong force chains explain the enhanced force anisotropy in dodecahedral packings. The combined contributions of all these features underlie the higher shear strength of packings of dodecahedra as compared with sphere packings.

These features highlight qualitative differences arising from particle shape, leading to:

1. an enhanced ortho-radial force anisotropy, resulting from the combined effects of friction mobilization and the projection of normal forces,
2. a negative branch vector length anisotropy, due to the alignment of face-to-face contacts along the compression axis,
3. a distinct role of triple contacts in amplifying force anisotropy.

Since the fabric anisotropy is similar for both particle shapes, it does not serve as a specific signature of shape effects. This suggests that the higher shear strength observed in dodecahedra does not stem from a fundamentally different organization of the contact network, but rather from local force balance mechanisms induced by particle geometry.

These results underline the necessity of considering particle shape effects when modeling granular materials. While spherical particles capture generic granular behavior, polyhedral particles exhibit distinct mechanisms at the particle scale that significantly impact macroscopic properties. A deeper understanding of non-spherical particle arrangements and their mechanical behavior will enhance our understanding of real granular materials. In an upcoming study, we will extend our analysis by incorporating new simulation data of additional regular polyhedral particles, such as icosahedra. We will explore the limits of fabric anisotropy imposed by steric exclusions between particles and the force balance condition. Furthermore, we will conduct a more detailed analysis of the influence of friction coefficient and particle shape on the limit fabric states.

We dedicate this paper to the memory of Professor Etienne Guyon, a dear friend and frequent visitor to our laboratories in the South of France. A passionate physicist deeply committed to cross-disciplinary research, he regarded grains and granular materials as both a unifying scientific field and a valuable pedagogical tool for understanding rheology [51].

Acknowledgements The authors acknowledge financial support by SIFCO project (CEA), EDF, and ORANO.

Data availability All relevant data are available upon request from the authors.

References

1. I. Agnolin, J.-N. Roux, Internal states of model isotropic granular packings. I. Assembling process, geometry, and contact networks. Phys. Rev. E **76**, 061302 (2007). https://doi.org/10.1103/PhysRevE.76.061302
2. P. Jop, Y. Forterre, O. Pouliquen, A constitutive law for dense granular flows. Nature **441**(7094), 727–730 (2006). https://doi.org/10.1038/nature04801
3. F. Radjai, J.-N. Roux, A. Daouadji, Modeling granular materials: century-long research across scales. J. Eng. Mech. **143**(4), 04017002 (2017)
4. T.-D. Tran, S. Nezamabadi, J.-P. Bayle, L. Amarsid, F. Radjai, Effect of interlocking on the compressive strength of agglomerates composed of cohesive nonconvex particles. Adv. Powder Technol. **36**(2), 104780 (2025). https://doi.org/10.1016/j.apt.2025.104780
5. T.-D. Tran, S. Nezamabadi, J.-P. Bayle, L. Amarsid, F. Radjai, Contact networks and force transmission in aggregates of hexapod-shaped particles. Soft Matter **20**(16), 3411–3424 (2024). https://doi.org/10.1039/D3SM01762A
6. D.C. Vu, L. Amarsid, J.-Y. Delenne, V. Richefeu, F. Radjai, Macro-elasticity of granular materials composed of polyhedral particles. Granul. Matter **26**(1), 6 (2023). https://doi.org/10.1007/s10035-023-01382-3
7. S. Zhao, J. Zhao, A poly-superellipsoid-based approach on particle morphology for dem modeling of granular media. Int. J. Numer. Anal. Methods Geomech. **43**(13), 2147–2169 (2019). https://doi.org/10.1002/nag.2951
8. Y.T. Feng, An energy-conserving contact theory for discrete element modelling of arbitrarily shaped particles: basic framework and general contact model. Comput. Methods Appl. Mech. Eng. **373**, 113454 (2021). https://doi.org/10.1016/j.cma.2020.113454
9. M. Boton, E. Azéma, N. Estrada, F. Radjai, A. Lizcano, Quasistatic rheology and microstructural description of sheared granular materials composed of platy particles. Phys. Rev. E **87**(3), 032206 (2013)
10. B. Saint-Cyr, K. Szarf, C. Voivret, E. Azéma, V. Richefeu, J.-Y. Delenne, G. Combe, C. Nouguier-Lehon, P. Villard, P. Sornay, Particle shape dependence in 2D granular media. EPL (Europhys. Lett.) **98**(4), 44008 (2012)
11. E. Azéma, F. Radjaï, R. Peyroux, G. Saussine, Force transmission in a packing of pentagonal particles. Phys. Rev. E **76**(1), 011301 (2007)
12. T. Börzsönyi, R. Stannarius, Granular materials composed of shape-anisotropic grains. Soft Matter **9**(31), 7401–7418 (2013)
13. A. Hafez, Q. Liu, T. Finkbeiner, R.A. Alouhali, T.E. Moellendick, J.C. Santamarina, The effect of particle shape on discharge and clogging. Sci. Rep. **11**(1), 1–11 (2021)
14. F. Radjai, F. Dubois, *Discrete-element Modeling of Granular Materials* (Wiley-Iste, Hoboken, 2011), p.425 https://hal.science/hal-00691805
15. H.M. Jaeger, Celebrating soft matter's 10th anniversary: toward jamming by design. Soft Matter **11**(1), 12–27 (2015)
16. L.K. Roth, H.M. Jaeger, Optimizing packing fraction in granular media composed of overlapping spheres. Soft Matter **12**, 1107–1115 (2016)
17. N. Govender, D.N. Wilke, C.-Y. Wu, J. Khinast, P. Pizette, W. Xu, Hopper flow of irregularly shaped particles (non-convex polyhedra): GPU-based DEM simulation and experimental validation. Chem. Eng. Sci. **188**, 34–51 (2018). https://doi.org/10.1016/j.ces.2018.05.011
18. M. Boton, N. Estrada, E. Azéma, F. Radjaï, Particle alignment and clustering in sheared granular materials composed of platy particles. Eur. Phys. J. E **37**, 1–8 (2014)
19. E. Azéma, F. Radjai, F. Dubois, Packings of irregular polyhedral particles: strength, structure, and effects of angularity. Phys. Rev. E **87**(6), 062203 (2013)
20. V. Richefeu, M.S. El Youssoufi, F. Radjaï, Shear strength properties of wet granular materials. Phys. Rev. E **73**(5), 051304 (2006)
21. L. Liu, S. Ji, Bond and fracture model in dilated polyhedral dem and its application to simulate breakage of brittle materials. Granul. Matter **21**(3), 41 (2019). https://doi.org/10.1007/s10035-019-0896-4
22. F. Radjai, V. Richefeu, Contact dynamics as a nonsmooth discrete element method. Adv. Dyn. Granul. Mater. **41**(6), 715–728 (2009)
23. D.C. Vu, L. Amarsid, J.-Y. Delenne, V. Richefeu, F. Radjai, Rheology and scaling behavior of polyhedral particle flows in rotating drums. Powder Technol. **434**, 119338 (2024). https://doi.org/10.1016/j.powtec.2023.119338
24. H.J. Herrmann, J.-P. Hovi, S. Luding, *Physics of Dry Granular Media*, vol. 350 (Springer, Berlin, 2013)
25. N.V. Brilliantov, F. Spahn, J.-M. Hertzsch, T. Pöschel, Model for collisions in granular gases. Phys. Rev. E **53**(5), 5382–5392 (1996)
26. M.Y. Louge, Computer simulations of rapid granular flows of spheres interacting with a flat, frictional boundary. Phys. Fluids **6**(7), 2253–2269 (1994)
27. M.P. Allen, D.J. Tildesley, *Computer Simulation of Liquids* (Oxford University Press, Oxford, 2017)
28. F. Radjai, Multi-periodic boundary conditions and the contact dynamics method. Comptes Rendus Mécanique **346**(3), 263–277 (2018)
29. P.-E. Peyneau, J.-N. Roux, Solidlike behavior and anisotropy in rigid frictionless bead assemblies. Phys. Rev. E **78**(4), 041307 (2008)

30. C. Heussinger, J.-L. Barrat, Jamming transition as probed by quasistatic shear flow. Phys. Rev. Lett. **102**, 218303 (2009). https://doi.org/10.1103/PhysRevLett.102.218303
31. P. Rissone, E.I. Corwin, G. Parisi, Long-range anomalous decay of the correlation in jammed packings. Phys. Rev. Lett. **127**, 038001 (2021). https://doi.org/10.1103/PhysRevLett.127.038001
32. Y. Wen, Y. Zhang, Fabric-based jamming phase diagram for frictional granular materials. Soft Matter (2024). https://doi.org/10.1039/D3SM01277H
33. G.D.R. MiDi, On dense granular flows. Eur. Phys. J. E **14**(4), 341–365 (2004)
34. Y. Forterre, O. Pouliquen, Flows of dense granular media. Annu. Rev. Fluid Mech. **40**(1), 1–24 (2008). https://doi.org/10.1146/annurev.fluid.40.111406.102142
35. A.N. Schofield, P. Wroth, *Critical State Soil Mechanics*, vol. 310 (McGraw-Hill, London, 1968)
36. D.M. Wood, *Soil Behaviour and Critical State Soil Mechanics* (Cambridge University Press, Cambridge, 1990)
37. L. Rothenburg, N.P. Kruyt, Critical state and evolution of coordination number in simulated granular materials. Int. J. Solids Struct. **41**(21), 5763–5774 (2004). https://doi.org/10.1016/j.ijsolstr.2004.06.001
38. N.P. Kruyt, L. Rothenburg, On micromechanical characteristics of the critical state of two-dimensional granular materials. Acta Mech. **225**(8), 2301–2318 (2014). https://doi.org/10.1007/s00707-014-1128-y
39. Y.F. Dafalias, Must critical state theory be revisited to include fabric effects? Acta Geotech. **11**, 479–491 (2016). https://doi.org/10.1007/s11440-016-0441-0
40. P.-E. Peyneau, J.-N. Roux, Frictionless bead packs have macroscopic friction, but no dilatancy. PRE **78**(1), 011307 (2008). https://doi.org/10.1103/PhysRevE.78.011307
41. R.J. Bathurst, L. Rothenburg, Observations on stress-force-fabric relationships in idealized granular materials. Mech. Mater. **9**(1), 65–80 (1990)
42. F. Radjai, J.-Y. Delenne, E. Azéma, S. Roux, Fabric evolution and accessible geometrical states in granular materials. Granul. Matter **14**(2), 259–264 (2012)
43. L. Staron, F. Radjai, Friction versus texture at the approach of a granular avalanche. Phys. Rev. E **72**(4), 041308 (2005)
44. J.-N. Roux, G. Combe, Quasistatic rheology and the origins of strain. Comptes Rendus Phys. **3**(2), 131–140 (2002). https://doi.org/10.1016/S1631-0705(02)01306-3
45. A. Taboada, N. Estrada, F. Radjaï, Additive decomposition of shear strength in cohesive granular media from grain-scale interactions. PRL **97**(9), 098302 (2006). https://doi.org/10.1103/PhysRevLett.97.098302
46. L. Rothenburg, R.J. Bathurst, Analytical study of induced anisotropy in idealized granular materials. Géotechnique **39**(4), 601–614 (1989). https://doi.org/10.1680/geot.1989.39.4.601
47. F. Radjai, H. Troadec, S. Roux, Key features of granular plasticity, in *Granular Materials: Fundamentals and Applications*, ed. by S.J. Antony, W. Hoyle, Y. Ding (Royal Society of Chemistry, 2004), pp. 157–184. Special Collection. ISBN: 978-0-85404-586-0. https://doi.org/10.1039/9781847550996-00157
48. F. Radjai, D.E. Wolf, M. Jean, J.-J. Moreau, Bimodal character of stress transmission in granular packings. Phys. Rev. Lett. **80**(1), 61–64 (1998)
49. C.-F. Zhao, N.P. Kruyt, An evolution law for fabric anisotropy and its application in micromechanical modelling of granular materials. Int. J. Solids Struct. **196–197**, 53–66 (2020)
50. C. Voivret, F. Radjaï, J.-Y. Delenne, M.S. El Youssoufi, Multiscale force networks in highly polydisperse granular media. PRL **102**(17), 178001 (2009). https://doi.org/10.1103/PhysRevLett.102.178001
51. E. Guyon, J.-Y. Delenne, F. Radjai, *Built on Sand: The Science of Granular Materials* (MIT Press, Cambridge, 2020)